Applied Physics B (2024) 130:22
https://doi.org/10.1007/s00340-023-08155-z

Applied Physics B
Lasers and Optics

RESEARCH

Design of convex-shaped transparent heat spreaders for symmetrical cooling of a thin-disk laser crystal by mechanical pressing

Jan-Hinnerk Wolter[1] · Andreas Voss[1] · Thomas Graf[1] · Marwan Abdou Ahmed[1]

Received: 24 September 2023 / Accepted: 28 November 2023 / Published online: 5 January 2024

Abstract
We present the design for a double-sided cooling of a thin-disk laser crystal using transparent, convex-shaped heat spreaders. The thermal contact between laser crystal and heat spreaders is established without bonding by solely applying an axial compressive force. A model of the contact behavior taking into account the deformation of the surfaces of the heat spreaders due to bending under mechanical loading is presented. The scope and accuracy of the modeling is verified by numerical simulations using the finite-element method. Based on the modeling, an exemplary design of the heat spreader which has been used for the first experimental demonstration of this concept is carried out. Based on the model, an almost ideal scalability of the heat transfer coefficient is predicted.

1 Introduction

The fields of application of lasers as tools in research and industry have expanded rapidly with the development of more powerful and more efficient radiation sources. Most of the progress was enabled by the development of modern diode-pumped laser concepts, which, starting with the rod laser, in particular have resulted in the fiber [1], slab [2] and thin-disk laser (TDL) [3]. For the TDL, in contrast to the other concepts, the excited volume can be increased in two dimensions via an easy-to-implement enlargement of the excited cross-section of the laser crystal at a constant pump power density without affecting the average temperature in the excited volume. This favorable scaling behavior of the TDL concept is based on the one-dimensional heat flow in the laser crystal, which typically has a thickness between 100 and 300 µm, leading to a higher thermal resistance than for cooling geometries using two- or three-dimensional heat flow, which, in turn, exhibit a less advantageous scalability. Despite this limitation to relatively low densities of heat generated in the crystal, the TDL can be operated very efficiently benefiting from the small fractional heating of Yb-doped laser crystals [4]. Using Yb:YAG for an oscillator an output power of 4 kW from one disk with an optical efficiency of 56% has been achieved in near-fundamental mode operation [5]. Due to the mentioned thermal limitation in combination with its short gain length, the TDL concept may be less favorable for laser crystals exhibiting very low emission cross-sections and short upper-state lifetimes and thus requiring very high absorbed pump power densities for efficient operation. In case of a co-occurrence of a large fractional heating, like in particular for the laser crystals doped with transition metals, laser operation becomes inefficient [6, 7] in comparison to the end-pumped rod concept. By all means, an improved TDL design offering a significantly decreased thermal resistance while largely retaining the scaling behavior is an attractive option for any high-power laser based on a suitable laser-active material, since a further increase in pump power density generally allows to extract a higher output power from a pump spot with a given diameter.

A straightforward approach to reduce the thermal resistance of the conventional TDL is to additionally cool the uncooled face of the laser crystal using a transparent heat spreader (THS), as demonstrated in [8]. In some similar looking configurations, as for example presented in [9], a cap made of sapphire or YAG is used to suppress the amplified spontaneous emission (ASE) of a R-TDL, but not primarily for optimizing the cooling. Due to the insufficient thermal conductivity of the materials used, the reduction of the thermal resistance is marginal. In other previous work using THSs to improve the cooling of lasers [10–13] the contact between the laser medium and the THS was established by

✉ Jan-Hinnerk Wolter
jan-hinnerk.wolter@web.de

[1] Institut für Strahlwerkzeuge (IFSW), Universität Stuttgart, Stuttgart, Germany

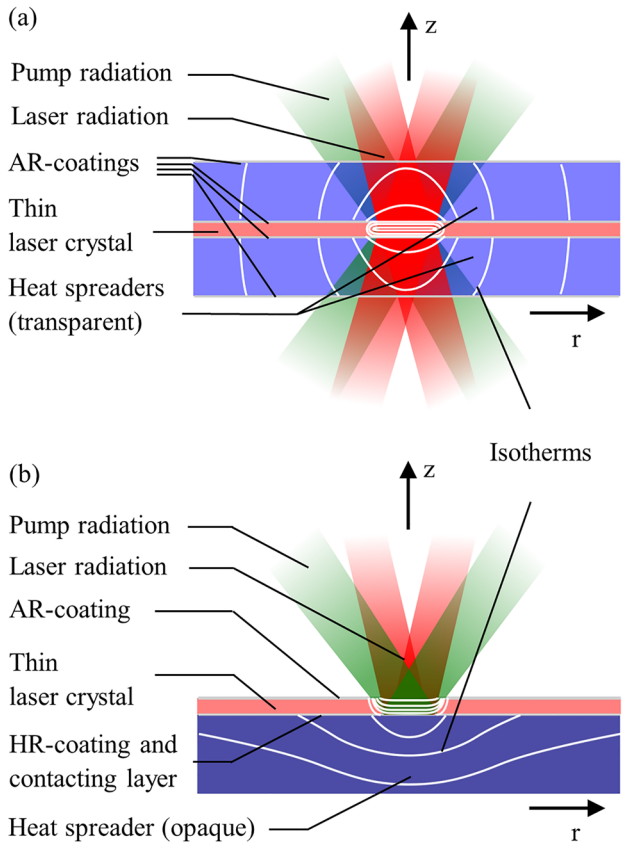

Fig. 1 Schematic cross-sectional views of the T-TDL concept (**a**) with cooling from both faces using THSs and of the R-TDL concept (**b**) with cooling of one face of the disk. The density and direction of the isotherms (white) indicate the magnitude and the direction, respectively, of the heat flow density within the laser crystal and the heat spreaders. The subsequent heat removal from the heat spreader, which takes place outside the optical path is not shown

either optical contacting, capillary or diffusion bonding of the uncoated contact surfaces. At cryogenic temperatures, the efficient operation of an Yb:YAG laser using THSs made of sapphire, exhibiting a high thermal conductivity at low temperatures, to cool a relatively thick laser crystal from both faces already has been demonstrated [10]. Unfortunately, the thermal conductivity of sapphire is dropping very strongly at higher temperatures; therefore, it is not a suitable choice for the THSs for cooling at room temperature. In contrast to the approach of improving a R-TDL by adding a THS, the symmetrical cooling of a thin laser crystal using two THSs fully exploits the potential.

2 Symmetrical thin-disk cooling

The schematic cross-section of the crystal arrangement of the symmetrically cooled TDL, also referred to as the transmissive thin-disk laser (T-TDL) is shown in Fig. 1a. Assuming the same thickness of the laser crystal, the resulting doubling of the cooled surface and the halving of the path length that the heat must travel before it is transferred to the heat spreaders leads to a reduction of the thermal resistance of the laser crystal by a factor of four compared to the conventional reflective thin-disk laser (R-TDL) approach, Fig. 1b. Since, in general, a significant difference in the refractive indices of the THS and the laser crystal exists, typically, anti-reflective (AR) coatings designed for both pump and laser wavelengths are required on the contacting surfaces for efficient pumping and laser operation without Fresnel losses. Otherwise, these losses can only be avoided by using the Brewster angle in the case of linearly polarized radiation, which limits the design of the resonator. In contrast, the R-TDL concept, as schematically shown in Fig. 1b, requires a highly-reflective (HR) coating and an adhesive or solder layer, ensuring a stable mechanical as well as thermal contact, on the cooled side of the disk. Since HR-coatings are typically one order of magnitude thicker than AR-coatings and both are generally made of materials having low thermal conductivities, avoiding the HR-coatings and contacting layers provides an additional thermal advantage for the symmetrical cooling concept.

In both disk laser concepts, the heat is transferred to the heat spreader essentially across the area of the pumped spot, which is small in comparison to the cooled area of the heat spreader. The spreading of the heat for a subsequent heat transfer with the largest possible area for the lowest possible contribution to the overall thermal resistance takes place with heat conduction in both the radial and axial direction. The overall thermal resistance is defined as the ratio of the temperature difference between the average temperature in the pumped volume of the laser crystal and the cooling temperature of the heat sink and the heating power generated within the laser crystal. In the case of R-TDLs, the heat transfer is typically achieved via an impingement flow of a coolant against the back of the heat spreader and therefore the heat flow inside the heat spreader occurs predominantly in axial direction, Fig. 1b. In contrast, in the case of the T-TDL, the cooled areas of the THSs have to be kept outside the clear aperture and therefore the heat flow is predominantly directed in the radial direction, cf. Fig. 1a. Since the proportion of the radially directed heat flow in the latter case is significantly larger, the thermal resistance of the heat spreader scales significantly worse. In order to achieve the best possible scalability of the overall thermal resistance of the cooling assembly, contributions scaling less then ideally, must be kept as small as possible. To this end, a material with an outstanding thermal conductivity must be chosen for the THSs. In comparison to the R-TDL, this aspect is much more crucial for a best possible scalability of the cooling assembly.

Since for surfaces with AR-coatings an insufficient permanent bonding strength was reported [13], the application of an axial compressive force is investigated in the following as an alternative approach for establishing a reliable contact between the AR-coated surfaces. This approach has been demonstrated for the first time for a solid-state laser crystal with a superior cooling efficiency compared to a R-TDL using Ti:sapphire for the laser crystal and single-crystal diamond for the THSs [14]. The demonstrated reduction of the overall thermal resistance significantly exceeds the four-fold reduction resulting from the contribution of the laser disk alone, as can be seen from the maximum absorbed pump power density at maximum output power. The aim of the present work is to significantly contribute to the revelation and exploitation of the full potential of this concept, that goes far beyond the potential which has been demonstrated by the first realization.

3 Comparison of T-TDL and R-TDL concept

It should be noted that to achieve this improvement, compared to the R-TDL, the effort for the pump optic is higher and a second parabolic mirror is required. Furthermore, due to additional restrictions for the guidance of the pump beam [14], depending on the thickness of the laser crystal, typically a pump source with a significantly higher brilliance is required. When, for example, a crystal having the same thickness as employed for the R-TDL is used, the number of beam passes through the crystal has to be doubled, which requires a total increase of the brilliance of the pump source by roughly a factor of 3 to 4. Moreover, to exploit the reduction of the thermal resistance to allow a corresponding increase in the pump power density, the brilliance of the pump source must be additionally increased by this reduction factor.

A comprehensive discussion of the pros and cons of the T-TDL concept in comparison to the R-TDL concept is complex and therefore clearly beyond the scope of this work. Instead, we present a comparison of two Yb:LuAG TDLs using laser crystals having the same thickness (e.g. 100 µm) and being able to generate the same amount of near-fundamental mode output power in the kilowatt range.

It should be noted that two prerequisites have to be fulfilled to realize the proposed T-TDL: firstly, large enough high-quality CVD diamond THSs (e.g. 15 mm diameter × 3 mm thickness) must be available. Secondly, the intracavity losses introduced by the THSs have to be low enough to allow almost the same extraction efficiency than with the R-TDL concept; for Yb:LuAG, due to its higher gain, this is much easier to achieve than for Ti:sapphire.

The at least fourfold increase in pump power density enabled by the double-sided cooling will allow to reduce the pump spot diameter by a factor of two or more (e.g. from 8 mm to less than 4 mm), which is a very substantial improvement with respect to the length of the dynamically stable resonator required for near-fundamental mode operation. In fact, a comparable resonator will be at least a factor of four more compact in the case of the T-TDL. This also substantially reduces the sensitivity of the laser setup to tilts of the resonator mirrors, e.g. induced by thermal effects. For the laser crystal, tilting is completely uncritical, since the laser beam passes it in transmission instead of being reflected at one of its surfaces, as in the case of the R-TDL; this also avoids the negative thermal lens due to the bending of the heat spreader observed in the case of the R-TDL.

At the same pump power density, the heat flow density per cooled side of the T-TDL is divided by a factor of two. Since the wavefront aberrations and the thermal lens caused by the heating of the laser crystal are proportional to the heat flow density and to the square of the average path length of the heat flow, which is divided by a factor of two also, they are reduced by a factor of eight per cooled side and by a factor of four for the complete crystal. Therefore, when quadrupling the pump power density, the wavefront aberrations and the thermal lens of the T-TDL laser crystal are nearly the same as in the case of the R-TDL operating at a four times lower pump power density.

As can be seen from the isotherms in Fig. 1a, the heat flow changes its direction from axial within the pump spot to almost radial outside the pump spot. The thermal lens in the THSs, therefore, roughly resembles that of an end-pumped rod laser with the important difference, that the heat conductivity in CVD diamond is more than 200 times higher than in Yb:LuAG. Consequently, this lens is quite weak (in the order of 0.03 Diopters for the example presented here) and, therefore, does not limit the dynamic stability of the resonator.

The significantly higher pump power density enabled by the T-TDL concept compared to a R-TDL using the same crystal thickness allows to reduce the pump spot diameter at the same output power. This lowers the radial gain for a given axial gain and therefore reduces the ASE losses in cw operation. However, the energy storage capability of the smaller pump spot is lower, since a smaller pumped volume requires a correspondingly higher inversion density to store the same amount of energy. The higher inversion causes a higher gain, leading to a stronger radial ASE despite the smaller pump spot. In principle, the THSs can be used as caps for suppressing the ASE. Unfortunately, to avoid reflections at near-normal incidence due to the refractive index difference between the laser crystal and the diamond THSs, typically, AR-coatings are required on the faces. Usually, these coatings are not designed to avoid reflections under large angles at the same time. Therefore, the ASE suppression is less than optimal when using AR-coatings.

In principle, it is possible to optimize the AR-coatings for large angles, too, but in this case, they would work correctly inside the contact area only, causing losses for laser radiation propagating outside the contact area.

Another significant advantage of the T-TDL is the strong reduction of the so-called air-wedge effect [15], which, in the case of the R-TDL, is caused by the heating of the ambient atmosphere in contact with the hot outer face of the laser crystal. The influence of this effect has either to be actively or passively compensated to achieve a stable output in high-power near-fundamental mode operation [16, 17]. Whereas in the case of the R-TDL, the surface in contact with the ambient air is the uncooled face of the disk, exhibiting the highest temperature of the laser disk, cf. Fig. 1b, in the transmissive concept, the outer faces of the THSs are in contact with the ambient air, cf. Fig. 1a, exhibiting a lower temperature than the lowest temperature of the laser disk and thus leading to a correspondingly strong reduction of the heating of the ambient air. Therefore, the T-TDL concept has a high potential to ease the realization of compact and robust thin-disk lasers delivering kilowatts of output power per crystal especially in high-brilliance and fundamental mode operation.

4 Operating principle

For the heat transfer between very smooth surfaces, as can be expected for optical components with dielectric coatings, there are several transport mechanisms to be considered [18]. The contribution to the heat transfer coefficient due to direct atomic contact, which stems from phonon diffusion in insulating bodies, requires a sub-nm distance. Even very high contact pressures are in practice still orders of magnitude smaller than the combined modulus of elasticity of the contacting hard bodies, which limits the direct contact area to a fraction of the order of 1% or less of the available nominal contact area [19]. Consequently, a constriction of the heat flow paths close to the surface is observed, giving rise to a so-called spreading resistance. The contributions to the heat transfer of the direct contact and the spreading resistance are both proportional to the nominal pressure [20]. For almost the complete apparent contact area, the surfaces are not in direct contact and the interfacial separation is typically in the order of magnitude of the combined surface roughness. Here, the relevant mechanisms of heat transport are due to capillary bridges formed by water, ballistic transport by air molecules, and evanescent electromagnetic waves [18]. Under typical ambient conditions, a one to two nm thick water film is present on the hydrophilic AR-coated surfaces and forms capillary bridges at the interface of the contacting surfaces. For roughness values in the range of a few nm or below, the contributions from ballistic transport and capillary bridges dominate the contribution from direct contact at low pressures of tens of MPa [18]. For an accurate estimation of the heat transfer coefficient, the topography of the surfaces in contact must be isotropic and the roughness power spectrum has to be known [19]. Regardless of this, the pressure dependency of each contribution to the heat transfer is, at least basically, known. The contributions of the direct contact and of the spreading conductance increase proportionally with increasing pressure. Due to their dependency on the interfacial separation, which—at least for self-affine fractal surfaces—decreases logarithmically with increasing pressure [21], the contributions of the capillary bridges and from evanescent electromagnetic waves increase as well. Beside the effort to reduce surface irregularities and the roughness of the THSs, which is also important to reduce scattering losses of the laser radiation, maximizing the contact pressure is, therefore, the key for improving the heat transfer. Another aspect to be considered for the contact resulting from the formation of capillary bridges is adhesion. The adhesion work begins to rise from zero if there is just enough water to fill the interfacial gap [22]. This is certainly not the case for the contacting surfaces of the THSs used in [14] under ambient conditions with rms roughness values larger than one nm. However, a further reduction in roughness might require adhesion to be taken into account, which would lead to a beneficial increase in contact force and contact radius.

To apply the contact in the case of the T-TDL concept, the necessary contact force has to be introduced in the THSs at a distance from the optical axis in order to leave the necessary clear aperture unobstructed as shown in Fig. 2a. In case of a plane THS and without thermal load, the mechanically applied pressure in this arrangement causes a deformation of the THS, which creates a contact area at the edge only, as can be seen in Fig. 2b. The contact at the center is established under thermal load only, whereby the temperature increase in the pumped volume of the laser crystal leads to a thermal expansion in axial direction, which is observed as a bulging of the laser crystal, as depicted in Fig. 2c. Since the thermal resistance of a thin disk typically is at least one order of magnitude higher for heat flow in the radial direction than in the axial direction, the contact area at the edge is irrelevant for the cooling of the laser crystal. To ensure the contact at the center of the disk, a convex shape of the THS is, therefore, considered as shown in Fig. 3a, so that the curvature due to deflection is counteracted by the shape of the THS [23]. When compared to the plane THS shown in Fig. 2, two main advantages are achieved by employing a convex-shaped THS. On one hand the contact area is ensured at the center of the laser crystal independent of the thermal load condition as can be seen in Fig. 3b, c. On the other hand, the contact pressure as well as the diameter of the contact area can be adjusted via the contact force, thus

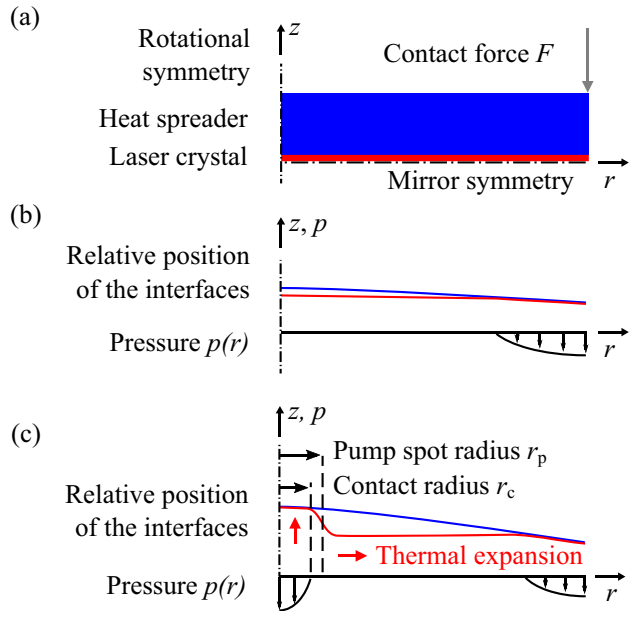

Fig. 2 Basic arrangement of contacting of the laser crystal and a plane heat spreader by using a contact force introduced at its edge (using rotational and mirror symmetry) (**a**); position of the interfaces and resulting pressure distributions on the laser disk without thermal load (**b**) and under thermal load (**c**)

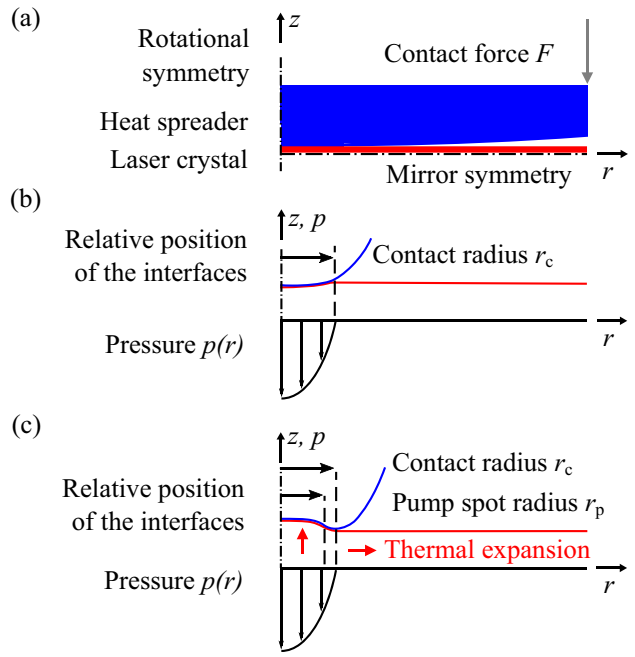

Fig. 3 Basic arrangement of contacting of the laser crystal and heat spreader by pressing using THSs with convex-shaped contact surfaces and a contact force introduced at its edge (using rotational and mirror symmetry) (**a**); position of the interfaces and resulting pressure distributions on the laser disk without thermal load (**b**) and under thermal load (**c**)

allowing to achieve an optimum contact pressure within the area of the pump spot.

Compared to the full-face contact established between laser crystal and THS by bonding methods, the advantage of restricting the contact area to the area required for the heat transfer is that shear stresses between the contact bodies due to the different thermal expansion in the radial direction are limited to a minimum. Regarding the cooling of the THSs, in principle, heat sinks can be directly mounted to their peripheral surface or to their flat outer surface. In this case, to ensure a sufficiently large area for the heat transfer, the diameter of the THSs has to be much larger than required for the clear aperture only. Therefore, due to the limited availability of large single-crystal diamond THSs, secondary heat spreaders (SHSs) made of polycrystalline diamond are used to transfer the heat from the THSs to the heat sinks.

5 Contact model

To describe the contact between the convex-shaped surfaces of the THSs with equal radii of curvature R_S and the plane thin laser crystal, a model using the method of dimensionality reduction (MDR) [24] is developed in the following, which enables a deeper insight into the working principle of the symmetrical cooling of the laser disk and also provides a useful tool for designing the THSs. In the following, the term "clamping" is used for two different types of fixture: in the first case, the laser crystal is clamped between two THSs by an axial clamping force; assuming negligible friction, the radial movement of the laser crystal is not suppressed. In the second case, the THS is fixed rigidly at its rim by SHSs; here, the movement and the bending of the edge of the THSs are suppressed strongly in all directions. As can be seen in Fig. 4, the THSs are clamped to SHSs, e.g. by soldering or by gluing. In the FEM simulations, a constant pressure acting on the outer face of the SHS was assumed and the clamping was realized as in the experiment, i.e. by implementing a radial overlap between the flat surfaces of the THS and the SHS. The use of the flat surface with a much higher possible surface quality than that of the peripheral surface leads to a better heat transfer and in addition allows to achieve a much larger contact surface, since the overlap between the two surfaces can be adjusted, which further improves the heat transfer. Moreover, the radial overlap increases the effective stiffness of the composite of the heat spreaders. Both the THSs and SHSs are deflected due to the finite stiffness of the composite of the heat spreaders in combination with the mechanical load condition shown in Fig. 4a.

For the contact model, the deflection of the THS is analytically described using plate theories [25, 26] for an equivalent mechanical load condition compared to Fig. 4a and a clamping to the SHS with a finite stiffness as shown

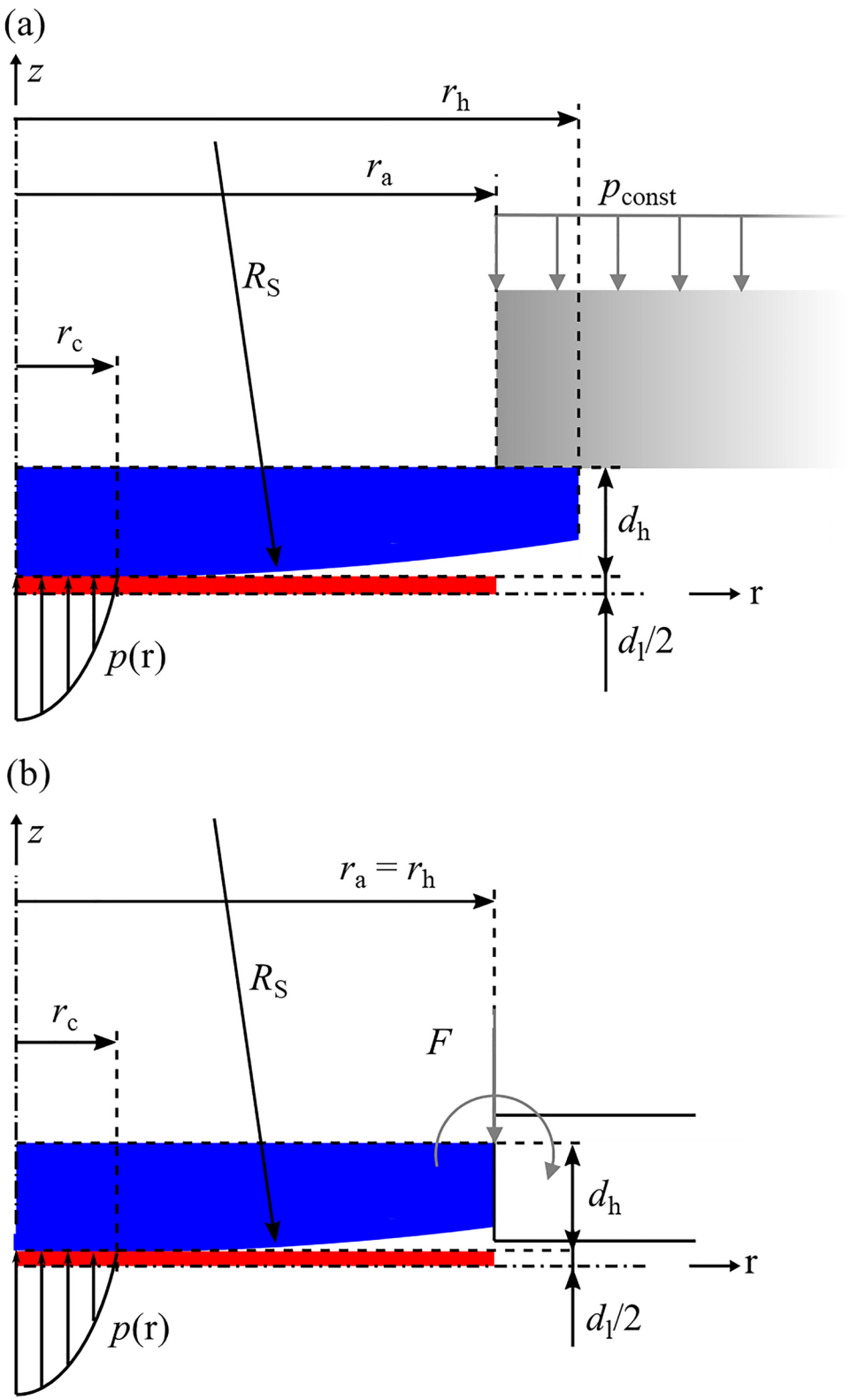

Fig. 4 **a** Experimentally realized geometry which was also used for the numerical calculations using FEM. The THS (blue) is clamped on the laser crystal (red) by the SHS (gray) with a radial overlap of $r_h - r_a$ and a constant pressure on the SHS. The thickness of the secondary heat spreader made of polycrystalline diamond was 2.0 mm and its outer radius r_o = 17.5 mm. **b** Simplified geometry used for the contact model with an equivalent mechanical load condition acting on the THS. r_h is the radius of the THS, R_S is the radius of curvature of the THS, r_a is the clamping radius of the THS, d_h is thickness of the THS, d_l is thickness of the laser crystal, p_{const} is the pressure on the SHS, F is the external clamping force, M is the bending moment, $p(r)$ is the pressure distribution between laser disk and THS and r_c is the contact radius

in Fig. 4b. The equivalent mechanical load condition acting on the THS at the position of the clamping consists of the force corresponding to the constant pressure acting on the SHS and a bending moment resulting from its radial displacement from the center of gravity of the pressure to the position of the clamping as shown in Fig. 4b. The bending moment leads to a rotation of the THS at the position of the clamping, which is proportional to the bending moment

and reciprocally proportional to the effective stiffness of the composite of both heat spreaders. The effective stiffness can either be calculated also within the framework of plate theory or, more precisely, evaluated from FEM calculations. The calculations using plate theory related to the composite of both heat spreaders must, however, be performed numerically, since the analytical solutions are no longer manageable. The approach of using an effective stiffness in the contact model is far superior compared to including the complete deflection of the composite, since the deflection of the THS can still be described analytically. Moreover, this approach allows much faster numerical calculations and it also is more adequate to the problem, since only the deflections of the THSs are of interest for the contact model. For an adequate description of the contact behavior, beside taking into account the deflection of the THS, also the spatial extent of the contacting bodies has to be considered. According to [24], the shape of the contact bodies plays a negligible role as long as their spatial extent in all directions is at least as large as the size of the contact area, since this volume makes the largest contribution to the force relation of the contact. This requirement is certainly not fulfilled for the thickness of the laser crystal. Very recently, a semi-analytical method was presented that allows contact problems between a rigid, arbitrarily shaped axisymmetric convex body and a thin elastic layer to be treated rigorously within the framework of the MDR, but not in the case that both bodies are elastic [27]. We, therefore, adopt the result of a reduced influence of the modulus of elasticity of a thin plate for a contact of a thin elastic plate pressed between two elastic spheres compared to a contact between a plane half-space against a sphere presented by Tu and Gazis [28, 29].

For the contact model, we use the description of a frictionless normal contact without adhesion. As a preliminary condition for applying the MDR, we state that the half-space approximation holds, since the contact radii are very small compared to the radius of curvature R_S of the curved surface of the THS, i.e. the contact radius $r_c \ll R_S$. Thus, the parabolic approximation, i.e. $r \ll R_s$, also holds, since $r \leq r_c$ [24] and the axisymmetric difference between the surface profiles reads

$$f(r) = \frac{r^2}{2R_s} + \frac{F}{D}\left(\overline{w}(r) - \overline{w}(0)\right), \tag{1}$$

where $\overline{w}(r) \geq 0$ is the normalized deflection curve given by

$$\overline{w}(r) = \frac{D}{F} w(r). \tag{2}$$

F is the external force, as shown in Fig. 4b, and D is the stiffness of the THS. Since $\overline{w}(0)$ is the maximum normalized deflection at the center of the disk, an increasing force reduces the difference between the surface profiles in Eq. (1). The stiffness of the THS is given by Eq. (2.14) in [25], which reads

$$D = \frac{{d_h}^3 {E_h}^*}{12}, \tag{3}$$

where d_h is the thickness and E_h^* is the modulus of elasticity with suppressed lateral contraction of the THS.

When applying Eq. (3), it has to be considered that the approximation of a virtually constant thickness of the THS is used. Provided that the radius of curvature R_S is in the range of meters (considering e.g. $R_S = 2.5$ m as the minimum value relevant for this work), the thickness of the THS is in the range of millimeters ($d_h \geq 0.5$ mm), and the clamping diameter $2r_a$ is in the range of one centimeter (assuming e.g. $r_a \leq 7$ mm), the variation of the thickness is less than 2% in the worst case to be considered here. Hence, the assumption of a constant thickness is justified in reasonable approximation for the cases discussed in this work.

Treating the THS as a thin, stiff plate within the framework of the classical plate theory (CPT) [25, 30] is a good approximation when the ratio $A = 2r_a/d_h$ between the clamping diameter and the thickness of the THS lies between 8 and 100 [25]. The deflection curve $w(r)$ caused by the bending and found by using the CPT describes the shape of the neutral axis of a thin plate and can be used as an approximation for the surface deformation of the THS. The validity of this approximation in the examined parameter range will be verified later below in Sect. 7. The deflection curve for any rotationally symmetric pressure distribution is calculated by applying the principle of superposition [25] to the deflection curve of a clamped plate under a concentrical line load. This results in

$$\overline{w}(r) = \frac{D}{F}\left[\int_0^r \frac{p(r_0)}{q_0} w_o(r, r_0) dr_0 + \int_r^{r_c} \frac{p(r_0)}{q_0} w_i(r, r_0) dr_0\right], \tag{4}$$

where p is the pressure distribution, q_0 is the magnitude of the line load at $r = r_0$, and w_o and w_i are the deflection curves for the outer and inner portion of the thin plate as solutions of the ordinary differential equation for the line load and the boundary condition of a clamping to the SHS with a finite stiffness. This implies an effective stiffness of the composite D_{eff} of the THS and SHS. Using the boundary conditions of a derivative of the deflection curve equalling $-M_q/D_{eff}$ with the moment $M_q = q_0 r_0 (r_s - r_a)$ at the position of the clamping and a vanishing deflection at the clamping, since any offset is irrelevant for the difference between the surface profiles according to Eq. (1), we found as solutions

$$w_o = \frac{q_0 r_0}{8 D {r_a}^2}\Big[\left({r_a}^2 + {r_0}^2\right)\left({r_a}^2 - r^2\right) - 2{r_a}^2\left({r_0}^2 + r^2\right)\ln\frac{r_a}{r} + \frac{4 D r_a (r_s - r_a)}{D_{eff}}\left({r_a}^2 - r^2\right)\Big], \tag{5}$$

$$w_i = \frac{q_0 r_0}{8 D {r_a}^2}\Big[\left({r_a}^2 - {r_0}^2\right)\left({r_a}^2 + r^2\right) - 2{r_a}^2\left({r_0}^2 + r^2\right)\ln\frac{r_a}{r_0} + \frac{4 D r_a (r_s - r_a)}{D_{eff}}\left({r_a}^2 - r^2\right)\Big], \tag{6}$$

where r_s is the center of gravity of the pressure distribution acting on the SHS. In the case of an infinite stiffness of the clamping, also the effective stiffness becomes infinite and Eqs. (5) and (6) then equal the results for a clamping to a rigid body given by Eqs. (4.37b) and (4.37a) in [25], respectively. As can be seen from Eq. (4), the difference between the profiles in Eq. (1), which is used in the MDR calculation procedure to determine the pressure distribution, depends on the pressure distribution in a non-trivial manner and thus the contact problem in general cannot be solved in a closed form.

To further investigate the problem but also to get suitable starting values for an iterative solution, we develop the deflection curve in a Taylor series around the center of the contact and then receive

$$f(r) = \frac{r^2}{2R_s} + \frac{F}{D}\left(\frac{\overline{w}^{(2)}}{2} r^2 + \frac{\overline{w}^{(4)}}{24} r^4 + \dots\right) \tag{7}$$

for Eq. (1), where $\overline{w}^{(n)}$ with even n are the non-zero Taylor coefficients. The transformed one-dimensional difference between the profiles is calculated according to Eq. (3.27) in [24], and reads

$$g(x) = \frac{x^2}{R_s} + \frac{F}{D}\left(\overline{w}^{(2)} x^2 + \frac{\overline{w}^{(4)}}{9} x^4 + \dots\right), \tag{8}$$

where x is the transformed coordinate. The relation between the contact force and the contact radius is calculated from Eq. (8) according to Eq. (3.33) in [24], and reads

$$F = \frac{4 E^* \gamma}{3 R_s} {r_c}^3 \left(1 + \frac{F R_s}{D}\left[\overline{w}^{(2)} + \frac{2\overline{w}^{(4)}}{15} {r_c}^2 + \dots\right]\right), \tag{9}$$

where the same notation for the contact force on the LHS and for the external force on the RHS is used, since both forces have to be equal when the bodies are in static contact without adhesion. E^* is the combined modulus of elasticity

$$\frac{1}{E^*} = \frac{1}{{E_h}^*} + \frac{1}{{E_l}^*}, \tag{10}$$

with suppressed lateral contraction of the laser disk, denoted by the index l, and the THSs, and γ is a correction factor, which must be added by multiplication to the RHS of Eq. (9) as introduced in the force relation of Eq. (42) in [28] in case of a finite thickness of the laser disk. This factor means a reduction in the influence of the modulus of elasticity of the thin plate compared to that of a half-space (Eq. (5.23) in [31]) and depends on the relative contact radius λ defined by the ratio of the contact radius r_c and half of the thickness of the plate $d_l/2$ [28]. From [29], it can be concluded that γ can be calculated by

$$\gamma\left({E_h}^*, {E_l}^*, \lambda\right) = \frac{1}{1 - \frac{2E^*}{{E_l}^*}\left(1 - \frac{1}{\gamma\left({E_h}^* = {E_l}^*, \lambda\right)}\right)}, \tag{11}$$

where $\gamma({E_h}^* = {E_l}^*, \lambda)$ is the correction factor in case of equal moduli of elasticity for the THSs and the thin laser disk, which can only be calculated numerically [28, 29]. From the course of curve A in the regime of a thin plate, i.e. for $1 < \lambda < \infty$, in Fig. 1 of [29], which shows $\gamma^{-1/3}$ versus $\gamma^{-1/3}\lambda^{-1}$, it is found that $\gamma({E_h}^* = {E_l}^*, \lambda)$ is well approximated by the function $2(1 + (C_1\lambda + C_2)^{-1})^{-1}$ with $C_1 = 0.396$ and $C_2 = 0.801$.

In case of sufficiently small contact radii, the Taylor coefficients with $n \geq 4$ can be omitted in Eq. (7), since $r \leq r_c$, and a parabolic difference between the profiles is found with an effective radius of curvature given by

$$\frac{1}{R_{eff}} = \frac{1}{R_s} + \frac{F}{D}\overline{w}^{(2)}. \tag{12}$$

It is worth mentioning, that if we further specify this case to that of two solid spheres and an infinite small thickness of the laser disk, R_{eff} becomes R_s due to the absence of bending, $1/\lambda$ approaches zero and thus γ becomes $1 + {E_h}^*/{E_l}^*$ according to Eq. (11). Then, Eq. (9) turns into the relation for the Hertzian contact of two equal spheres [31] as required. Conversily, in the limit of an infinite thickness of the laser disk, which corresponds to λ approaching zero, γ becomes one and Eq. (9) turns into the relation for the Hertzian contact between a sphere and a plane half-space [31].

After resolving Eq. (9) for the force, we receive the force relation of the contact problem, which reads

$$F\left(r_c\right) = \frac{\frac{1}{R_s}}{\frac{3}{4\gamma E^* {r_c}^3} - \frac{1}{D}\left(\overline{w}^{(2)} + \frac{2\overline{w}^{(4)}}{15} {r_c}^2 + \dots\right)}. \tag{13}$$

Finally, the pressure distribution is calculated from Eq. (8) according to Eq. (3.37) in [24], which results in

$$p(r) = \frac{2\gamma E^* r_c}{\pi R_S}\left(1 - \frac{r^2}{{r_c}^2}\right)^{1/2} \cdot \left(1 + \frac{F R_s}{D}\left[\overline{w}^{(2)} + \frac{2}{27}\overline{w}^{(4)}\left({r_c}^2 + 2r^2\right) + \dots\right]\right). \tag{14}$$

In the parabolic approximation, the pressure distribution of the Hertzian contact problem results as expected. With increasing contact radii, higher order Taylor coefficients must be taken into account to maintain a certain accuracy. Then, the maximum of the pressure distribution shifts away

from the center of the contact. As mentioned before, the only efficient direction for extracting the heat from the disk is the axial direction; due to this, the heat transfer must occur through the faces of the disk within the pumped area. Thus, taking into account the mentioned dependence of the contact resistance from the contact pressure, the contact pressure within the pumped area is the key parameter for an efficient heat transfer. It can, therefore, be concluded that there must be an optimum force for achieving an optimum cooling of the laser disk and consequently an optimum output power of the laser.

Using Eq. (4), we find

$$\overline{w}^{(2)} = \frac{D}{F}\int_0^{r_c} \frac{p(r_0)}{p_0}\, w_i^{(2)}\Big|_{r=0} dr_0 \tag{15}$$

for the first non-zero Taylor coefficient. Using the force $F_{\overline{w}^{(2)}}$ and pressure distribution $p_{\overline{w}^{(2)}}$ found in the parabolic approximation of the difference between the profiles, the Taylor coefficient $\overline{w}^{(2)}$ is calculated to be

$$\overline{w}^{(2)} = \frac{1}{20\pi}\left[5\left(\ln\frac{r_c}{r_a} + \ln 2 - \frac{5}{6} - \frac{(r_s - r_a)}{r_a}\frac{2D}{D_{\text{eff}}}\right) - \frac{{r_c}^2}{{r_a}^2}\right] < 0, \tag{16}$$

and thus the contact problem is solved in closed form in this case. For an iterative solving approach of the equations used in the MDR calculation procedure taking into account the complete deflection curve of the THS, the force $F_{\overline{w}^{(2)}}$ and pressure distribution $p_{\overline{w}^{(2)}}$ found with the parabolic approximation of Eq. (7) are reasonable starting values.

Since the contacting concept causes a significant amount of stress inside the THS, the design of the THS has to take into account this aspect. In particular, it has to be ensured that the maximum stresses to be expected are well below the fracture strength of the material. For brittle crystalline materials, tensile stress is known to be most critical. Its maximum $\sigma_r(r = 0)$ is found at the center of the outer face of the THS, where the maximum bending moment occurs. With Eq. (44) and Eq. (52) in [30] this maximum tensile stress yields

$$\sigma_{\text{tensile,max}} = -\frac{6F(1+\nu_h)\overline{w}^{(2)}}{{d_h}^2}. \tag{17}$$

According to the maximum normal stress (MNS) theory, brittle materials fail when the largest magnitude of the principal tensile stress exceeds the tensile strength of the material [32], i.e., $\sigma_{\text{tensile,max}} > \sigma_{ts}$. From Eqs. (13) and (17), it can be concluded that the radius of curvature given by the shape must fulfil the condition

$$R_s > \frac{\frac{-6(1+\nu_h)\overline{w}^{(2)}}{{d_h}^2}}{\sigma_{ts}\left(\frac{3}{4\gamma E^* {r_c}^3} - \frac{1}{D}\left[\overline{w}^{(2)} + \frac{2\overline{w}^{(4)}}{15}{r_c}^2 + \ldots\right]\right)}, \tag{18}$$

to avoid damage due to fracture. In practice, the nominal maximum stress should be significantly lower to take into account e.g. intrinsic stress or imperfections such as microcracks, etc.

Furthermore, tangential tensile stress in the unpumped volume of the laser disk, caused by the unequal thermal expansion in the pumped and in the unpumped volume in combination with the forces induced by the clamping, may also lead to fracture damage; this aspect has to be addressed in future work.

It is worth mentioning that the mechanical stress inside the THS, predominantly induced by the applied clamping force, may lead to significant induced birefringence, which in turn causes significant depolarization losses when using polarized radiation. Especially for laser-active materials allowing to achieve low small-signal gain coefficients only, these losses can reduce the efficiency of laser operation to a similar extent as for rod-type lasers, where the birefringence results from thermally induced stresses [33]. In order to significantly reduce these losses, a method was found that enables the mutual compensation of the depolarization of the radiation in the THSs if the thickness of the laser disk can be designed as a zero or multiple order half-wave plate for the laser radiation [34].

6 Validation of the contact model

To examine the scope of validity and accuracy of the contact model, the results of the model are compared with numerical calculations using FEM. For this purpose, it is convenient to normalize the contact force and the pressure distribution to the results of a solid sphere, which reads

$$F_n = \frac{3FR_s}{4\gamma E^* {r_c}^3}, \text{and} \tag{19}$$

$$p_n = \frac{2\pi p {r_c}^2}{3}\cdot\frac{F_n}{F}. \tag{20}$$

Then, it also becomes convenient to normalize the maximum tensile stress, contact radius and radial position according to

$$\sigma_{n,\text{tensile,max}} = \sigma_{\text{tensile,max}}\frac{{d_h}^2}{F}, \tag{21}$$

$$r_{c,n} = 2\left(\frac{2\gamma E^*}{{E_h}^*}\right)^{1/3}\frac{r_c}{d_h}, \text{and} \tag{22}$$

$$r_\mathrm{n} = 2\left(\frac{2\gamma E^*}{E_\mathrm{h}^*}\right)^{1/3}\frac{r}{d_\mathrm{h}}. \tag{23}$$

After normalization, the force relation of Eq. (13) reads

$$F_\mathrm{n}\left(r_\mathrm{c,n}\right) = \frac{1}{1 - r_\mathrm{c,n}^3\left(\overline{w}^{(2)} + \frac{\overline{w}^{(4)}}{30}\left(\frac{E_\mathrm{h}^*}{2\gamma E^*}\right)^{2/3} d_\mathrm{h}^2 r_\mathrm{c,n}^2 + \ldots\right)}, \tag{24}$$

and the pressure distribution of Eq. (14)

$$p_\mathrm{n}\left(r_\mathrm{n}\right) = \left(1 - \frac{r_\mathrm{n}^2}{r_\mathrm{c,n}^2}\right)^{\frac{1}{2}} \cdot \left(1 + F_\mathrm{n} r_\mathrm{c,n}^3 \cdot \left[\overline{w}^{(2)} + \frac{\overline{w}^{(4)}}{54}\left(r_\mathrm{c,n}^2 + 2r_\mathrm{n}^2\right)\left(\frac{E_\mathrm{h}^*}{2\gamma E^*}\right)^{2/3} d_\mathrm{h}^2 + \ldots\right]\right). \tag{25}$$

Both normalized quantities are independent of the radius of curvature of the THSs, but still dependent on the thickness of the THSs even in the parabolic approximation via the Taylor coefficient $\overline{w}^{(2)}$, however, the strongest dependency is on the normalized contact radius.

For the exemplary calculations presented in the following sapphire is considered as the material of the laser crystal and single-crystal diamond for the THSs. Due to its unique properties, especially the highest thermal conductivity of all materials at room temperature, a high transparency, and an exceptional elastic modulus, single-crystal diamond can be regarded as the most suitable material for THSs [35]. THSs with a reasonable range of aspect ratios with $A = 3.5$, 7.0 and 14.0 for a clamping radius of $r_\mathrm{a} = 3.5$ mm and radii of curvature R_S equal to 2.5, 5.0 and 10.0 m have been investigated in the numerical calculations. In the FEM calculations, in contrast to the contact model, the contact force is an independent variable and the range of the contact force was, therefore, specified in such a way that resulting contact radii ranged between 10 and 50% of the clamping radius. In Fig. 5, the normalized contact force calculated with the model using both the complete difference between the profiles or with only its parabolic approximation are compared with the results from FEM. For the iterative numerical approach to solve the contact model, the optimal implementation of the MDR was used according to [36]. The force $F_{\overline{w}^{(2)}}$ and pressure distribution $p_{\overline{w}^{(2)}}$ evaluated using the parabolic approximation were chosen as starting values in Eq. (1), and a relative change of the force between iterations of less than 10^{-3} was used as a termination criterion. As shown in Fig. 5, due to the normalization, the contact force of the model is independent of the radius of curvature. The normalization also works for the FEM results, as can be seen from the fact that the results for different radii of curvature become equal in this representation.

As can be seen in Fig. 5, by taking into account the complete difference between the profiles, the model overestimates the forces by less than 10%, while in the parabolic approximation of the difference between the profiles the forces are underestimated by 10% at maximum. The effective stiffness was calculated from the deflection of the THS at the position of the clamping from the FEM results, which linearly depends on the moment as predicted by Eqs. (5) and (6). The calculation of the effective stiffness using the CPT gives significantly worse results and thus can only give a rough estimation. In the worst case of the thickest THS, the effective stiffness calculated from the CPT is only 60% of the value determined from FEM. Although the stepwise radially varying thickness of the composite can be taken into account in the plate theories, the variation of the axial position of the neutral axis—within as well as between the radial segments—is completely ignored. In particular, the change in the position of the neutral axis due to the radial

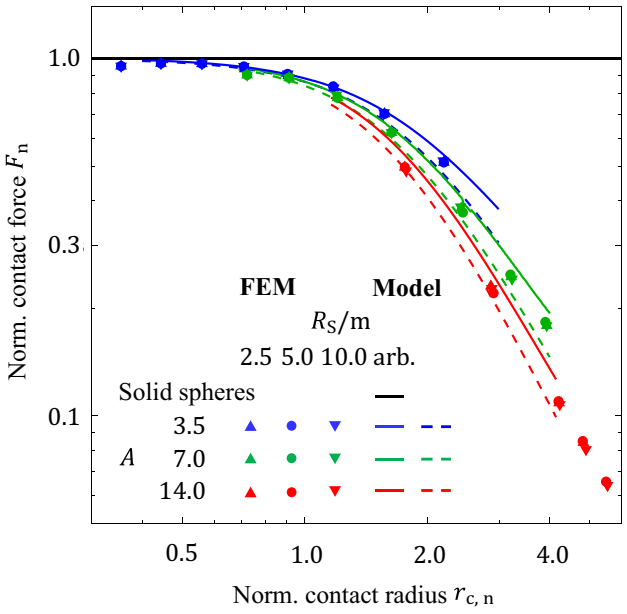

Fig. 5 Normalized contact force versus the normalized contact radius for the contact model taking into account the complete difference between the profiles (solid lines) or only its parabolic approximation (dashed lines) compared to numerical calculations (data points) using FEM in double logarithmic representation. The aspect ratios were realized with thicknesses of 2.0, 1.0 and 0.5 mm and a clamping radius of 3.5 mm. Each curve of the contact model is drawn for the contact radius ranging between 0.3 mm and 1.8 mm. The thickness of the laser disk was 0.15 mm, as used in [14]. The horizontal line represents the case of a thin plate pressed between two solid spheres, where deflection does not occur. The FEM calculations (COMSOL Multiphysics 5.2) were performed using the geometry shown in Fig. 4a. Single-crystal diamond was assumed for the THS and sapphire for the laser crystal with $E_\mathrm{h} = 1050$ GPa, $\nu_\mathrm{h} = 0.1$ [35] and $E_\mathrm{l} = 435$ GPa, $\nu_\mathrm{l} = 0.3$ [37], respectively. The effective stiffness of the composite of THS and SHS D_eff including their radial overlap was determined from the moment-dependent derivative of the difference between the profiles at the position of the clamping from the FEM calculations for which 7.13 kNm, 1.79 kNm and 0.48 kNm was found for the three composites

overlap of both heat spreaders as shown in Fig. 4a cannot be captured by plate theories. As seen in Eqs. (5) and (6), due to its solely parabolic contribution, the effective stiffness only influences the force relation of the contact and not the pressure distribution. Moreover, the influence depends on the ratio D/D_{eff}. In the case of the THS with the largest aspect ratio, the ratio D/D_{eff} is about 0.02. The clamping can therefore be assumed as ideally stiff in good approximation; accordingly, the results are hardly influenced when D_{eff} is set to infinity. In contrast, for the smallest aspect ratio of the THS, the value of D/D_{eff} is about 0.10. In this case, using the accurate value of D_{eff} from the FEM results is found to be crucial to attain the same accuracy of the force relation compared to the largest aspect ratio.

It is known that for aspect ratios below about 10, deflections are underestimated in the CPT and additional shear deformations have a significant contribution to the overall deformation [26]. Therefore, we also investigated the plate deformation in the first-order shear deformation theory (FSDT) [26], for which we found $q_0 r_0 {d_\mathrm{h}}^2/(6(1-\nu_\mathrm{h})K_\mathrm{S})\ln(r_\mathrm{a}/r_0)$ and $q_0 r_0 {d_\mathrm{h}}^2/(6(1-\nu_\mathrm{h})K_\mathrm{S})\ln(r_\mathrm{a}/r)$ as additional terms for the case of the concentrical line load, which are added to w_i and w_o in Eqs. (5) and (6), respectively, and where K_S is the shear correction factor. This result was verified by carring out the superposition of Eq. (4) for examples given in [26] for which we found equal results (Eq. (9.2.37) and Eq. (9.2.39) in [26]). However, using this FSDT solution for the plate deflection in the contact model only leads to improvements of the normalized force for relatively large normalized contact radii exceeding two. In contrast to the CPT results, the FSDT results exhibit an asymptotic behavior toward smaller normalized contact radii deviating significantly from the FEM results. Therefore, for the description of the deflection of the THSs, we adhere to the results based on the CPT, which are accurate enough for typical design requirements.

Another aspect found in Fig. 5 is that for sufficiently small normalized contact radii smaller than approximately 0.6, the bending of the THS can be neglected and the contact force reaches about 95% of the value obtained for solid spheres. For the studied range of the contact radii, this regime is only reached in the case of the smallest aspect ratio of 3.5. The normalized pressure distributions calculated with the model using both the complete difference between the profiles and its parabolic approximation are compared with numerical results from FEM for normalized contact radii ranging between one and four in Fig. 6a–d. The normalized contact radius is the dominant parameter influencing the normalized pressure distributions; the dependence on the aspect ratio is minor. As seen in Fig. 6a and b, even for small normalized contact radii, where the parabolic approximation holds well, there are differences between the FEM results and the model, which remain comparable even for higher

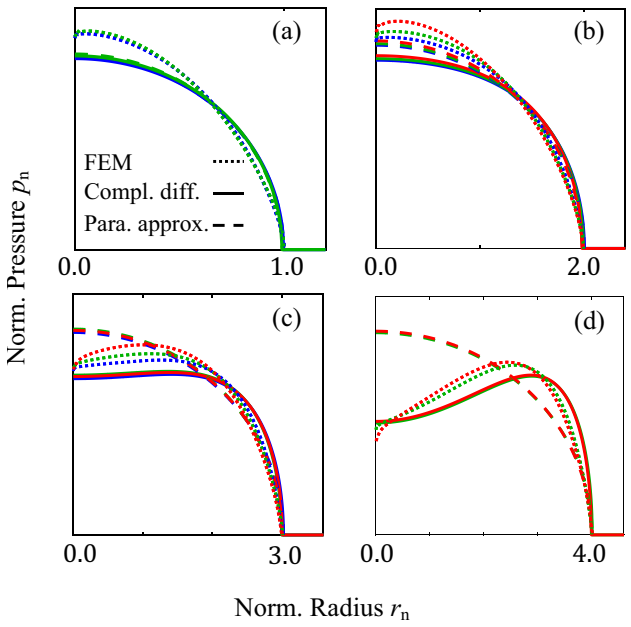

Fig. 6 Normalized pressure distributions versus the normalized radius for normalized contact radii of 1, 2, 3 and 4 shown in **a**, **b**, **c** and **d**, respectively, resulting from FEM (dotted), from the model taking into account the complete difference between the profiles (solid) and the model with only its parabolic approximation (dashed). To facilitate the comparison of the differences, the normalized pressure distributions have additionally been normalized to correspond to the same contact force for each normalized contact radius. The radius of curvature for these calculations was 5.0 m. All other parameters and the color code are the same as used for the calculations for Fig. 5. Please note, that the curves for the largest and smallest aspect ratio are not shown for the smallest and largest normalized contact radius, respectively, since the corresponding contact radii were not within the investigated range

normalized contact radii for the model using the complete difference between the profiles, as seen in Fig. 6c and d. These deviations can be understood by taking into consideration the basic assumptions made for the used formulas: firstly, the formulas assume that the externally applied forces are evenly distributed within the volume of the bodies; this is inconsistent with the boundary conditions of the investigated setup, where the external forces are locally applied at the rim of the THSs. Secondly, the FEM results take into account the slight modifications of the pressure distributions due to the finite thickness and stiffness of the laser disk, as can be seen in Fig. 2 in [29], which are ignored in the model. On the other hand, for the parameter ranges investigated here, the deflection of the surface of the THS is reasonably well approximated by the deflection of the neutral axis, since the relative displacement in the radial direction of the surface of the THS is in the range of 10^{-4} at maximum and thus can be neglected; the same holds for the change of the thickness of the THS due to lateral contraction. Therefore, this approximation does not contribute significantly to the remaining

differences between the FEM results and the model. Nevertheless, the results obtained using the contact model are sufficiently accurate for typical design requirements. For larger normalized contact radii shown in Fig. 6c and d, the pressure distributions resulting from the model using the parabolic approximation increasingly deviate from the FEM results. The contact model using the complete difference between the profiles is, however, capable of reproducing the main features of the pressure distributions also for higher normalized contact radii, which is characterized by an increasing pressure drop in the center as expected from Eq. (25). For the very large normalized contact radius of 5.2, which is only reached for the highest aspect ratio of 14.0 in this study and corresponds to a contact radius of only 1 mm, a lift-off of the contact at the center is observed in the FEM calculations. This regime cannot be explored with the contact model, since the MDR requires a simply connected contact area [24]. We observed that the convergence of the calculations becomes increasingly slow for normalized contact radii exceeding four.

The normalized maximum tensile stress is shown in Fig. 7 as a function the normalized contact radius. The largest deviation between the FEM and the contact model of up to of 50% is found for the smallest aspect ratio. Since the THSs have to be designed such that the maximum tensile stress

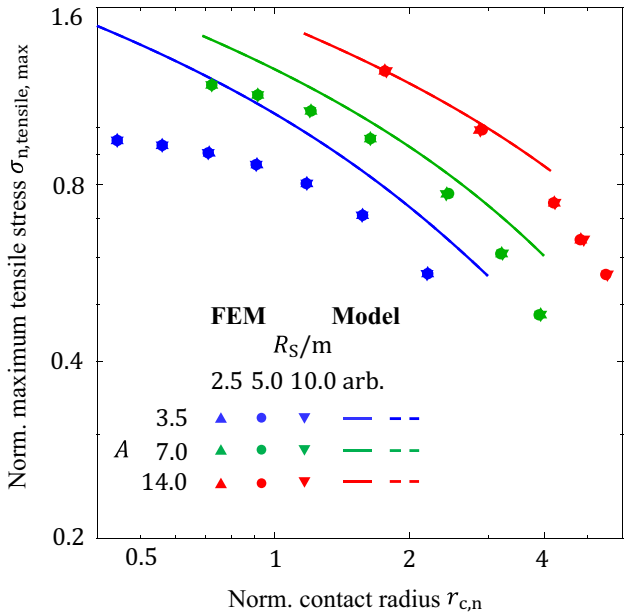

Fig. 7 Normalized maximum tensile stress at the center of the THS versus the normalized contact radius resulting from FEM (data points) and from the model in double logarithmic representation. The curves taking into account the complete difference between the profiles (solid lines) and only its parabolic approximation (dashed lines) coincide due to the normalization of the maximum tensile stress. The same parameters as for the calculations for Fig. 5 were used

is well below the tensile strength, typically by one order of magnitude, this accuracy can be regarded as sufficient.

In conclusion, it can be summarized that up to a normalized contact radius of about two, it is sufficient to use the contact model with the parabolic approximation of the difference between the profiles, as seen in Figs. 5 and 6. Only for larger normalized contact radii, the pressure distribution is described more precisely by using the complete difference between the profiles.

7 Example for the design of the heat spreaders

In the following, we describe the design for the first implementation of this concept as reported in [14], where single-crystal diamond was chosen for the THSs and Ti:sapphire for the laser crystal. For this setup, two pump spot diameters of 2.3 mm and 1.2 mm were considered. The required clear aperture of at least three times the pump spot diameter led to a clamping diameter of 7 mm. To ensure a sufficiently wide radial overlap between the THS and the heat sink, in this case at least 2.5 mm, an outer diameter of 12 mm was chosen for the THSs. To further distribute the heat before the subsequent removal by microchannel coolers but also to provide the necessary stiffness for the clamping of the THSs, ring-shaped secondary heat spreaders made from polycrystalline diamond were used. These rings had a thickness of 2 mm and an outer diameter of 35 mm and were glued to the THSs with a very thin bond line, similar to the gluing used for R-TDLs. The microchannel coolers were simply pressed by the clamping force against the secondary heat spreaders. As seen from Eqs. (13) and (14), in order to maximize the pressure for an optimum heat transfer between laser disk and THS, the stiffness of the THS, which strongly depends on the thickness, must be maximized. The maximum available thickness of 1.0 mm was therefore chosen, which was limited due to current production technology, leading to an aspect ratio of 7.0. Since no information on the roughness power spectra of the convex-shaped surfaces of the single-crystal diamond THSs used in [14] is available, it is unfortunately not possible to make accurate estimations of the heat transfer coefficient as well as of its pressure dependency for this special case. The range for the total heat transfer coefficient from the laser crystal to the THS including the thermal layer resistance of the AR-coatings can, however, be estimated. With a thickness of the coatings of 370 nm and a thermal conductivity of the dense sputtered coatings of about 1 W/(mK) [38], the heat transfer coefficient for two coatings in series is $1.4 \cdot 10^6$ W/(m^{2}K), which determines the upper limit for the total heat transfer coefficient. By taking into account a minimum heat transfer coefficient at the interface given by ballistic transport of air of $3 \cdot 10^5$ W/(m^{2}K) [18], the lower

limit of the total heat transfer coefficient yields $2.5 \cdot 10^5$ W/(m^{2}K). Due to the not exactly known, but certainly significant contribution of capillary bridges, the actual value is assumed to be substantially higher.

To estimate the optimum contact force for a maximized heat transfer between the laser disk and the THS, it is necessary to consider a quantity which is representative for the pressure in the entire pumped cross-section of the laser disk. As a reasonable and easy to calculate quantity, we use the mean pressure within the pumped cross-section

$$p_\mathrm{m} = \frac{1}{\pi {r_\mathrm{p}}^2} \int_0^{r_\mathrm{p}} 2\pi p(r) r dr. \tag{26}$$

We are interested in the maximum of the mean pressure, however, neither the optimum force nor the corresponding optimum contact radius can be stated explicitly. Also, the optimum force will deviate to a certain extent from the force for an optimum laser operation since effects as for instance diffraction losses are not taken into account. Determining the force for maximum output power theoretically is a demanding task and beyond the scope of this work, but it is comparatively easy to determine experimentally.

For studying the mean pressure, the interdependence of the product of the mean pressure and the radius of curvature $p_\mathrm{m}R_\mathrm{S}$ and the product of the contact force and the radius of curvature FR_S may be considered, since the RHS of Eq. (13) then becomes independent of R_S and the RHS of Eq. (14) then depends on FR_S but not on R_S alone. For the two pump spot diameters, these quantities were calculated using the contact model and compared with FEM calculations as shown in Fig. 8a and b, respectively. The maxima of the mean pressure are fairly broad for both sizes of the pump spot in the unpumped case. The values of FR_S at the maximum of $p_\mathrm{m}R_\mathrm{S}$ for the smaller pump spot diameter predicted by the model and the FEM calculation are 375 Nm and 400 Nm, respectively. For the larger pump spot diameter, the model and the FEM calculation predict a maximum for contact forces of 700 and 800 Nm, respectively. As a compromise for the first realization of this concept [14], a value of $FR_\mathrm{S} = 600$ Nm was chosen as a working point in order to operate the laser with both pump spot diameters without the need for any mechanical readjustment in the first experiment.

In the last following step, we now determine the radius of curvature R_S. As seen in Eq. (13), R_S must be minimized to maximize the force and thus the peak pressure, but the tensile strength of the material sets a lower limit according to Eq. (18). Using a quite conservative value for the tensile strength of single-crystal diamond of $\sigma_\mathrm{ts} \approx 1.5$ GPa [35], the minimum radius of curvature according to Eq. (18) is calculated to be $R_\mathrm{S,min} = 0.25$ m. Here, a quite conservative choice of $R_\mathrm{S} = 5.0$ m was made, which corresponds to a safety factor of 20 against failure due to fracture. With this

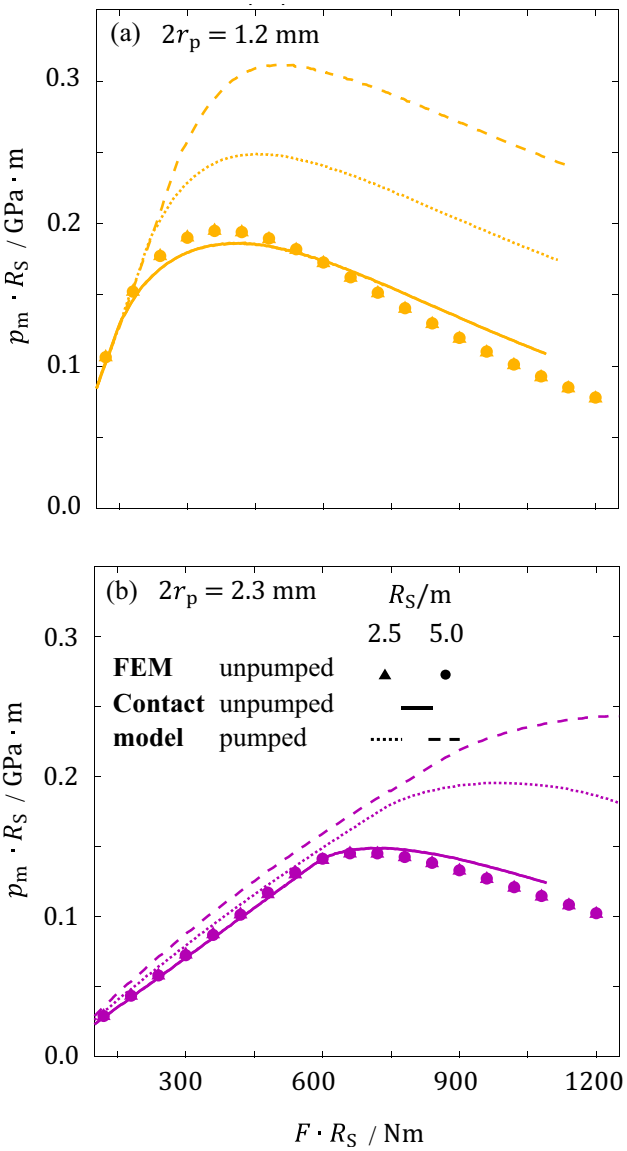

Fig. 8 The product of mean pressure and radius of curvature $p_\mathrm{m}R_\mathrm{S}$ versus the product of contact force and radius of curvature FR_S calculated with FEM and using the contact model as described in the previous section for the unpumped and pumped case for **a** the small pump spot and **b** the large pump spot. Single-crystal diamond with a thickness of $d_\mathrm{h} = 1.0$ mm was assumed for the THSs and sapphire with a thickness of $d_\mathrm{l} = 150$ µm was assumed for the laser disk. The radius of curvature is either $R_\mathrm{S} = 2.5$ m or $R_\mathrm{S} = 5.0$ m and the clamping radius is $r_\mathrm{a} = 3.5$ mm

choice for the radius of curvature, the contact force yields $F = 120$ N. Under pumping, the temperature rise in the laser crystal leads to a modification of the difference between the profiles of the contacting surfaces of both the laser disk and the THSs due to thermal expansion, hereinafter referred to as thermal bulging $b_\mathrm{th}(r)$. In contrast to established laser cooling concepts, thermal bulging thus does not only affect the operation of the laser by thermal lensing and diffraction

losses but also via an influence on the pressure-dependent heat transfer between the laser crystal and the THSs, since a modification of the difference between the profiles is related to a modification of the pressure distribution as stated by the MDR [24].

Following the calculation procedure of the MDR, the thermally induced force F_{th} and pressure distribution p_{th} are calculated from the thermally induced difference between the profiles $f_{\mathrm{th}}(r) = b_{\mathrm{th}}(0) - b_{\mathrm{th}}(r)$ and can simply be added to the force and pressure distribution found for the unpumped case for any contact radius due to the linear elasticity of the materials [24]. Under the assumption that partially suppressed lateral contraction can be neglected, the thermal bulging can be calculated by

$$b_{\mathrm{th}}(r) = \int_0^{\frac{d_{\mathrm{l}}}{2}} \alpha_{\mathrm{l}}(T)\big(T(r,z) - T_{\mathrm{sink}}\big)dz + \int_{\frac{d_{\mathrm{l}}}{2}}^{\frac{d_{\mathrm{l}}}{2}+d_{\mathrm{h}}} \alpha_{\mathrm{h}}(T)\big(T(r,z) - T_{\mathrm{sink}}\big)dz, \tag{27}$$

where α_{l} and α_{h} are the coefficients of linear thermal expansion of the laser disk and the THSs, respectively. The calculation of the temperature field required for Eq. (27) necessitates the knowledge of the pressure dependence of all heat transfer mechanisms involved and thus is a complex thermo-mechanically coupled task, which can only be carried out if the surface is isotropic and the roughness power spectrum is known [19]. Therefore, due to the lack of these surface data, a reasonable estimation of the thermal bulging will be employed in order to investigate its impact on the contact between laser disk and the THSs. For the estimation of the height of the thermal bulge using Eq. (27), we consider that the thermal conductivity of diamond is about two orders of magnitudes higher than the one of sapphire. Then, the second term in Eq. (27) can be neglected, since, firstly, the temperature variation in the THS within the volume limited in the radial direction by the radius of the pump spot is small compared to the temperature variation in the laser crystal, and secondly, the coefficient of linear thermal expansion of diamond is more than five times smaller than the one of sapphire despite the fact that the thickness of the THS is about one order of magnitude larger than the thickness of the laser crystal. Moreover, for the remaining first term in Eq. (27), the temperature distribution in the laser disk is replaced by the average temperature. Then, the height of the thermal bulge is estimated by

$$\Delta b_{\mathrm{th}} \approx \alpha_{\mathrm{l}}\big(T_{\mathrm{m}} - T_{\mathrm{sink}}\big)\frac{d_{\mathrm{l}}}{2}. \tag{28}$$

Using a maximum temperature of 80 °C as estimated for Ti:sapphire from [6], a heat sink temperature of −13 °C as used in [14], and a coefficient of linear thermal expansion of sapphire of $5.2 \cdot 10^{-6}\mathrm{K}^{-1}$ [37], the height of the thermal bulge is found to be about 36 nm.

To estimate the radial dependence of the bulging, we consider a supergaussian function of 3rd and 4th order for the small and the large pump spot radius, respectively, which are reasonable approximations to describe the bulging of the laser crystal of a R-TDL with the same thickness of the laser crystal and supergaussian pump distributions of 6th order as calculated using the calculation procedure presented in [39]. Therefore, the thermal bulge is estimated by

$$b_{\mathrm{th}}(r) \approx \Delta b_{\mathrm{th}}\left\{1 - \exp\left[-\log 2\left(\frac{r}{r_{\mathrm{p}}}\right)^{n}\right]\right\}, \tag{29}$$

where n is the order of the supergaussian distribution. The estimated thermal bulges are shown in Fig. 9.

As a consequence of the thermal bulging, a quite substantial enhancement of the mean pressure is observed, as shown in Fig. 8a, b. Despite the significant increase of the mean pressures, a rather moderate shift of the optimum contact forces is found. The values of FR_{S} at the maximum of $p_{\mathrm{m}}R_{\mathrm{S}}$ for the pumped case for the smaller pump spot diameter predicted by the model are 450 and 480 Nm corresponding to contact radii of 0.91 and 0.93 mm for the small and the large radius of curvature, respectively. For the large pump spot diameter, the model predicts a maximum of $p_{\mathrm{m}}R_{\mathrm{S}}$ for contact forces of 950 and 1200 Nm corresponding to contact radii of 1.30 and 1.33 mm for the small and the large radius of curvature, respectively. For the nominal contact force of 120 N, the pressure distributions are depicted for the unpumped and for the pumped case for both pump spot sizes in Fig. 10a

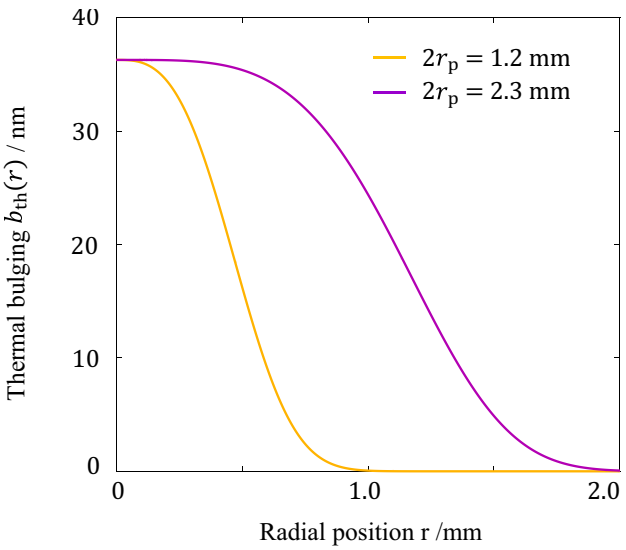

Fig. 9 Estimated thermal bulging b_{th} of the laser disk for pump spot diameters of 1.2 mm and 2.3 mm assuming an average temperature of 80 °C in the pumped volume of the laser disk and a heat sink temperature of −13 °C calculated from Eqs. (28) and (29). All other parameters are the same as stated under Fig. 8

and b. Since the resulting level of contact pressure in the pumped case is uncritical for both contact partners, a further increase can in principle be considered. When e.g. reducing the radius of curvature to $R_S = 2.5$ m, the maximum pressure increases by a factor of two, which is still well within the safe region in case of single-crystal diamond. An additional increase of the thickness to $d_h = 2.0$ mm, which reduces the normalized contact radius for the unpumped case to $r_{c,n} = 1.4$, would increase the contact force about two times, as can be read from Fig. 5, and therefore, leads to an additional twofold increase of the mean pressure. Also, the contribution of the THSs to the overall thermal resistance is significantly reduced. However, the potential for further increasing the mean contact pressure is very limited, since the bending of the THS is already largely suppressed and the reduction in the radius of curvature is limited by the tensile stresses that occur.

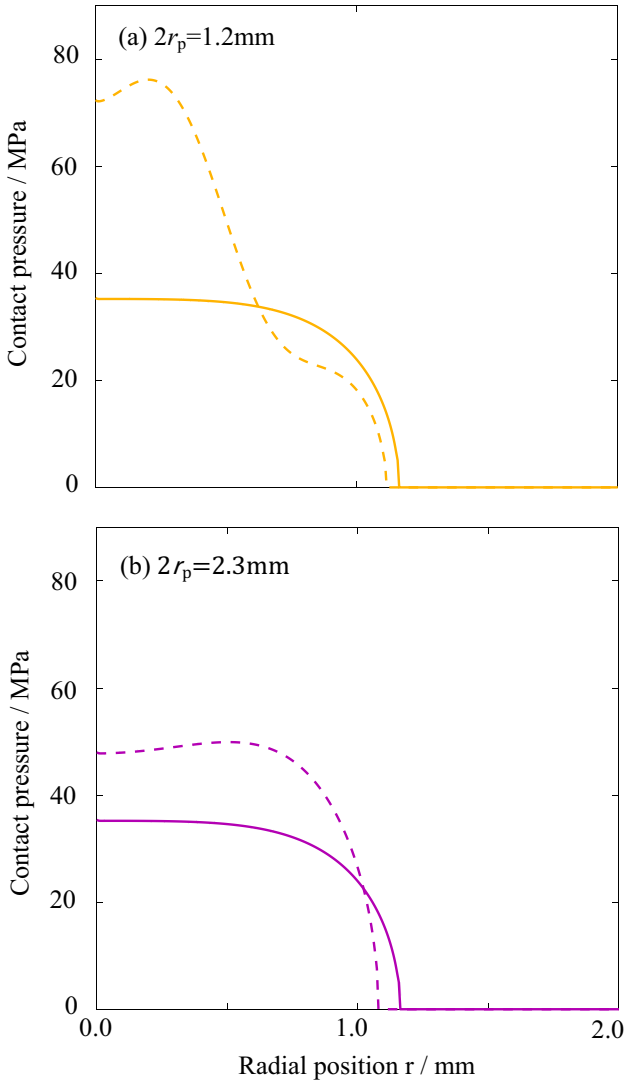

Fig. 10 Pressure distributions for the unpumped (solid) and pumped case (dashed) for **a** a pump spot diameter of 1.2 mm and **b** a pump spot diameter of 2.3 mm for a contact force $F = 120$ N and a radius of curvature of $R_S = 5.0$ m. All other parameters are the same as stated under Fig. 8

8 Discussion

We have presented the basic design principles for cooling of a thin disk-shaped laser crystal by pressing it between two convex-shaped, transparent heat spreaders (THSs). A contact model was developed, which provides a good qualitative understanding of the contact behavior and a sufficient accuracy for estimating the optimum parameters for the design of the THSs. The validity of the model has been checked for a reasonable range of aspect ratios as well as radii of curvature of the THSs numerically by FEM.

Under thermal load, a significant increase of the mean pressure is found due to the bulging of the laser crystal. However, as demonstrated for the exemplary design, the differences between the optimum contact forces predicted by the model for the unpumped and the pumped case are small enough to make the model for the unpumped case sufficiently accurate for estimating the optimum design parameters.

For several reasons, the cooling concept becomes particularly advantageous when the thickness of the THS is sufficiently large compared to the pump spot diameter. Most obviously, a sufficiently thick THS minimizes its contribution to the overall thermal resistance. Since the optimum contact radius is larger than the pump spot radius, the normalized contact radius also becomes small. This ensures that the contact force and thus the peak pressure is close to the theoretical limit of a solid sphere, as can be seen in Fig. 5, and also that a pressure drop at the center of the contact is prevented, as can be seen from Fig. 6. Simultaneously, the variation of the pressure distribution within the pump spot is minimized. This can be concluded from the exemplary designs, for which the ratios between thickness and pump spot diameter are 0.83 and 0.43 and the normalized contact radii are 2.0 and 2.9 for the smaller and the larger pump spot diameter, respectively. As can be deduced from Fig. 8a and b, at the maximum of the mean pressure, the contact radii extend beyond the pump spot radii by a factor of 1.5 and 1.2, respectively. Thus, the pressure drop at the edge of the pump spot with respect to the pressure in the center is smaller for the smaller pump spot, for which the ratio between the thickness of the THS and the pump spot diameter is larger. As already mentioned above, the SHSs play an essential role both for the mechanical as well as for the thermal performance of the setup. In particular, to fully exploit the pressure level which can be achieved with the THSs, the SHSs have to be significantly thicker than the THSs.

While studying the factors determining the performance of the T-TDL concept in detail, it became obvious that the surface roughness of the contacting surfaces plays a crucial role not only for efficient laser operation, but for optimum heat extraction as well. For example, a reduction of the roughness of the convex surfaces of the THSs by a factor of three compared to the first experimental realization [14] would not only reduce the scattering losses—which are especially critical in case of a low small-signal gain—by an order of magnitude, but simultaneously would also reduce the width of the gap by a factor of three, which would allow the water film on the surfaces under normal conditions to fill the entire gap in the apparent contact area [18], thus improving the heat transfer at the interface significantly.

Finally, the model shall be used to assess the scalability of the thermal resistance of the heat transfer between the laser disk and the THS, since this is an important prerequisite for the scalability of the overall thermal resistance of the T-TDL concept. In the following, doubling the size of the pump spot is considered as a simple, yet representative case of power scaling. To maintain the required minimum clear aperture, the clamping radius must also be doubled. When applying this magnification to all other geometrical parameters of the design as well, i.e. thickness and radius of curvature of the THSs and the contact radius, the contact force increases depending on the dominating term in the denominator of Eq. (13) by a factor between four and $4\gamma(2\lambda)/\gamma(\lambda)$, which is at maximum 4.8 in the case of diamond for the heat spreader and sapphire for the laser disk. Since the thickness of the laser disk is conserved, the normalized contact radius is increased by $(\gamma(2\lambda)/\gamma(\lambda))^{1/3}$ according to Eq. (22), which is found to be less than 1.07, and therefore is almost conserved. Thus, the same holds for the shape of the pressure distribution, as can be seen in Fig. 6. Consequently, the mean pressure increases by a factor between one and $\gamma(2\lambda)/\gamma(\lambda)$ according to Eq. (26) and also the maximum tensile stress according to Eq. (17). When the resulting minor increase of the tensile stress is tolerable, by adapting the specified geometrical parameters and the contact force as described an ideal scalability of the heat transfer at the contact interfaces is achieved. Therefore, provided that the contribution of the thermal interface between the THSs and the heat sinks to the overall thermal resistance can be kept sufficiently small, ultimately only the radial heat conduction within the heat spreaders will limit the scalability of this cooling concept.

Acknowledgements The research leading to these results has received funding from the European Union Seventh Framework Programme (ICT-2013.3.2-Photonics) under grant agreement no. 619177 in the project 'TiSa TD'.

Author contributions J-HW prepared the first draft version; J-HW and AV intensively discussed the draft versions and refined it iteratively; J-HW developed the contact model, performed all calculations and prepared all figures. J-HW took the lead in writing the manuscript supported by AV. TG and MAA supervised and led the planning and implementation of research activities. All authors reviewed the manuscript.

Funding Open Access funding enabled and organized by Projekt DEAL. This article is funded by Seventh Framework Programme, 619177.

Data availability The datasets generated and/or analyzed during the current study are available from the corresponding author on request.

Declarations

Conflict of interest The authors declare no competing interests.

References

1. E. Snitzer, J. Appl. Phys. **32**, 1 (1961)
2. J. Eggleston, T.T. Kane, K. Kuhn, J. Unternahrer, R. Byer, IEEE J. Quantum Elect. **20**, 3 (1984)
3. A. Giesen, H. Hügel, A. Voss, K. Wittig, U. Brauch, H. Opower, Appl. Phys. B **58**, 365–372 (1994)
4. T.Y. Fan, IEEE J. Quantum Elect. **29**(6), 1457–1459 (1993)
5. S.S. Schad, V. Kuhn, T. Gottwald, V. Negoita, A. Killi, K. Wallmeroth, Solid State Lasers XXIII: Technol. Devices **8959**, 156–161 (2014)
6. J.H. Wolter, M. Abdou Ahmed, T. Graf, Opt. Lett. **42**, 8 (2017)
7. G. Renz, J. Speiser, A. Giesen, I.T. Sorokina, E. Sorokin, Solid State Lasers Xxii: Technol. Devices **8599**, 310–316 (2013)
8. P. Millar, A.J. Kemp, D. Burns, Opt. Lett. **34**, 6 (2009)
9. I. Kuznetsov, A. Pestov, I. Mukhin, M. Volkov, M. Zorina, N. Chkhalo, O. Palashov, Opt. Lett. **45**, 2 (2020)
10. S. Tokita, J. Kawanaka, Y. Izawa, M. Fujita, T. Kawashima, Adv. Solid-State Photonics (TOPS) **98**, 628–632 (2005)
11. H. Kahle, C.M.N. Matteo, U. Brauch, P. Tatar-Mathes, R. Bek, M. Jetter, P. Michler, Optica **3**, 12 (2016)
12. Z. Yang, D. Follman, A.R. Albrecht, P. Heu, N. Giannini, G.D. Cole, M. Sheik-Bahae, Elec. Lett. **54**, 7 (2018)
13. G.A. Newburgh, A. Michael, M. Dubinskii, Opt. Express **18**, 16 (2010)
14. J.H. Wolter, R. Balmer, S. Ricaud, M. Antier, C. Simon-Boisson, T. Graf, M.A. Ahmed, Laser Phys. Lett. **17**, 1 (2019)
15. J.P. Negel, A. Loescher, A. Voss, D. Bauer, D. Sutter, A. Killi, A.M. Abdou, T. Graf, Opt. Express **23**, 16 (2015)
16. T. Dietrich, S. Piehler, C. Roecker, M. Rumpel, M.A. Ahmed, T. Graf, Opt. Lett. **42**, 17 (2017)
17. A. Diebold, F. Saltarelli, I.J. Graumann, C.J. Saracenco, C.R. Phillips, U. Keller, Opt. Express **26**, 10 (2018)

18. B.N.J. Persson, B. Lorenz, A.I. Volokitin, Eur. Phys. J. E **31**, 1 (2010)
19. B.N.J. Persson, Surf. Sci. Rep. **61**, 4 (2006)
20. B.N.J. Persson, J. Phys.: Cond. Matter. **26**, 1 (2013)
21. B.N.J. Persson, Phys. Rev. Lett. **99**, 12 (2007)
22. B.N.J. Persson, Cond. Matter. **20**, 315007 (2008)
23. J. H. Wolter, A. Voss: US patent 10840669B2
24. V.L. Popov, M. Heß, *Method of dimensionality reduction in contact mechanics and friction* (Springer Vieweg, Berlin, Heidelberg, 2015)
25. E. Ventsel, T. Krauthammer, E.J.A.M.R. Carrera, *Thin plates and shells: theory, analysis, and applications* (Marcel Dekker, New York, Basel, 2001)
26. C.M. Wang, J.N. Reddy, K.H. Lee, *Shear deformable beams and plates* (Elsevier Science, Oxford, 2000)
27. F. Forsbach, Machines **11**, 4 (2023)
28. Y. Tu, D.C. Gazis, J. Appl. Mech. **31**, 4 (1964)
29. Y. Tu, J. Appl. Mech. **34**, 2 (1967)
30. S. Timoshenko, S. Woinowsky-Krieger, *Theory of plates and shells* (McGraw-Hill, New York, 1987)
31. V.L. Popov, *Kontaktmechanik und Reibung* (Springer Vieweg, Berlin, Heidelberg, 2015)
32. W.F. Riley, L.W. Zachary, *Introduction to mechanics of materials* (John Wiley & Sons, New York, 1989)
33. W.A. Clarkson, N.S. Felgate, D.C. Hanna, Opt. Lett. **24**, 12 (1999)
34. J. H. Wolter. A. Voss: US patent 10608398B2
35. R.S. Balmer, J.R. Brandon, S.L. Clewes, H.K. Dhillon, J.M. Dodson, I. Friel, P.N. Inglis, T.D. Madgwick, M.L. Markham, T.P. Mollart, N. Perkins, G.A. Scarsbrook, D.J. Twitchen, A.J. Whitehead, J.J. Wilman, S.M. Woollard, J. Phys.: Cond. Matter **21**, 36 (2009)
36. J. Benad, Facta. Univ. Ser: Mech. Eng. **16**, 2 (2018)
37. E.R. Dobrovinskaya, *Sapphire – material, manufacturing, applications* (Springer, Boston, 2009)
38. S.M. Lee, D.G. Cahill, T.H. Allen, Phys. Rev. B **52**, 1 (1995)
39. N. Hodgson, A. Caprara, Appl. Opt. **55**, 36 (2016)